IOP Publishing New J. Phys. 26 (2024) 013043 https://doi.org/10.1088/1367-2630/ad1a28

New Journal of Physics
The open access journal at the forefront of physics

Deutsche Physikalische Gesellschaft DPG
IOP Institute of Physics

Published in partnership with: Deutsche Physikalische Gesellschaft and the Institute of Physics

OPEN ACCESS

RECEIVED
23 September 2023

REVISED
27 November 2023

ACCEPTED FOR PUBLICATION
3 January 2024

PUBLISHED
23 January 2024

PAPER

Realizing quantum speed limit in open system with a $\mathcal{PT}$-symmetric trapped-ion qubit

Pengfei Lu[1,5], **Teng Liu**[1,5], **Yang Liu**[1,2,5], **Xinxin Rao**[1], **Qifeng Lao**[1], **Hao Wu**[1], **Feng Zhu**[1,2] and **Le Luo**[1,2,3,4,*]

[1] School of Physics and Astronomy, Sun Yat-sen University, Zhuhai 519082, People's Republic of China
[2] Shenzhen Research Institute of Sun Yat-Sen University, Nanshan Shenzhen 518087, People's Republic of China
[3] State Key Laboratory of Optoelectronic Materials and Technologies, Sun Yat-Sen University, Guangzhou 510275, People's Republic of China
[4] International Quantum Academy, Shenzhen 518048, People's Republic of China
[5] These authors contributed equally to this work.
[*] Author to whom any correspondence should be addressed.

E-mail: luole5@mail.sysu.edu.cn

Keywords: quantum speed limit, non-Hermitian system, quantum control, trapped-ion

Abstract

Quantum speed limit (QSL), the lower bound of the time for transferring an initial state to a target one, is of fundamental interest in quantum information processing. Despite that the speed limit of a unitary evolution could be well analyzed by either the Mandelstam–Tamm or the Margolus–Levitin bound, there are still many unknowns for the QSL in open systems. A particularly exciting result is about that the evolution time can be made arbitrarily small without violating the time-energy uncertainty principle, whenever the dynamics is governed by a parity-time ($\mathcal{PT}$) symmetric Hamiltonian. Here we study the QSLs with both $\mathcal{PT}$ and anti-$\mathcal{PT}$ Hamiltonians, and pose the QSL as a brachistochrone problem on a non-Hermitian Bloch sphere. We then use dissipative trapped-ion qubits to construct the Hamiltonians, where the state evolutions reach the QSL governed by a generalized Margolus-Levitin bound of the non-Hermitian system. We find that the evolution time monotonously decreases with the increase of the dissipation strength and exhibits chiral dependence on the Bloch sphere. These results enable a well-controlled knob for speeding up the state manipulation in open quantum systems, which could be used for quantum control and simulation with non-unitary dynamics.

1. Introduction

Quantum speed limit (QSL) is a fundamental concept in quantum mechanics, which describes how fast a system could evolve from an initial state $|\psi_i\rangle$ to a target state $|\psi_f\rangle$. The QSL plays an essential role in the fields of quantum computing [1–3], quantum communication [4], quantum metrology [5, 6], quantum non-equilibrium thermodynamics [7], and quantum coherent control [8, 9]. In a closed system, the fastest evolution is bounded by the limit of $\tau = \max(\tau_{\rm MT}, \tau_{\rm ML})$, where the Mandelstam-Tamm bound $\tau_{\rm MT} = \pi\hbar/2\Delta E$ [10–13] and the Margolus–Levitin bound $\tau_{\rm ML} = \pi\hbar/2\langle E\rangle$ [14, 15], relating the maximum speed of evolution to the energy uncertainty and the mean energy of the system respectively.

Despite the well-established limit for the unitary dynamics, there does not exist a single standard for the QSL in open systems, due to the complexity of the coupling between the system and the environment. In recent years, intensive theoretical studies have been devoted to explore how fast an open quantum system can evolve [16–27]. One of the particular examples is that for a non-Hermitian $\mathcal{PT}$-symmetric system, the state transfer can speedup and the flipping time will approach to an infinitesimal time scale without violating the time-energy uncertainty principle [28, 29]. Meanwhile, both $\mathcal{PT}$ [30, 31] and anti-$\mathcal{PT}$- symmetric non-Hermitian Hamiltonian [32, 33] have been experimentally constructed in trapped ions. In this paper, we report the first experimental study of the QSL in the $\mathcal{PT}$-symmetric system of trapped ions with controllable state-dependent dissipation coupled to the diagonal terms of the Hamiltonian.

It is noted that the speedup of the non-Hermitian system has been experimentally explored in the optical cavity quantum electrodynamics (QED) [34] and the two-qubit nuclear magnetic resonance system [35], but the speedup mechanism is quite different with that of our experiments. In the former, the speedup is due to the environment induced coupling to the coherence terms which is the off-diagonal terms of the Hamiltonian. In the latter, the speedup is the result of the post-selection of the non-Hermitian subspace of the unitary evolution of the two qubits.

In this work, we first map the non-Hermitian Hamiltonians to a variant Bloch sphere modified by the $\mathcal{CPT}$ theorem [28]. By choosing the evolution along the geodesic lines on the sphere, we demonstrate that the speed of the state transfer in a single $^{171}Yb^{+}$ ion qubit is beyond the QSL of the unitary evolution. The maximum speed matches the extended ML bound in open system derived from the Bures metric approach. It is noted that the trapped-ion experiments have already realized the state transfer of picosecond time scale [36, 37], where the absolute speed is much faster than our results. But those speeds still remain within the QSL of the unitary dynamics, and the fast evolution is due to the strong coupling strength with the ultrafast lasers. Instead, our result is obtained with standard microwave pulses, where the QSL under the unitary dynamics is surpassed due to the non-Hermitian term of the dissipation.

2. Results and discussion

2.1. Construction of the $\mathcal{PT}$ Hamiltonian with trapped-ion qubits

In order to experimentally study the speedup evolution enabled by the $\mathcal{PT}$-symmetric quantum theory, we construct a passive $\mathcal{PT}$-symmetric system with the energy levels of the trapped $^{171}Yb^{+}$ ion [31, 33], as shown in figure 1(a). The ion can be initialized to either $|0\rangle = |F=0, m_F=0\rangle$ or $|1\rangle = |F=0, m_F=1\rangle$ in $^2S_{1/2}$ electronic ground state. A microwave with the frequency of 12.643 GHz is used to couple the two spin states. A 369.5 nm laser beam with π polarization and adjustable intensity is employed as a dissipation beam to excite the ion from $|1\rangle$ to $|F=0, m_F=0\rangle$ in $^2P_{1/2}$ electronic excited state. The ion will spontaneously decay to either one of the three ground states ($|F=1, m_F=0, \pm 1\rangle$) of $^2S_{1/2}$ with the same probability. This configuration can be simplified to a two-level open system $|0\rangle$ and $|1\rangle$, with $|a\rangle = |F=1, m_F \pm 1\rangle$ taken as the environment. The population of state $|1\rangle$ or $|0\rangle$ is measured by the standard fluorescence counting rate threshold method. But, in this experiment, the population in $|1\rangle$ cannot be detected directly because the population of $|1\rangle$ and $|a\rangle$ are simultaneously pumped by the detection beam which contains both $\sigma_{\pm}$ and π polarization. Instead, we first apply an extra Rabi π pulse to exchange the population of $|0\rangle$ and $|1\rangle$, then detect the total population of $|1\rangle$ and $|a\rangle$ using the detection beam. Since the population in all involving states remains unity, we could infer the population of $|0\rangle$, which is the initial population of $|1\rangle$ before the exchange. The experimental setup for non-Hermitian trapped-ion qubits is detailed in appendix A.

The two-level open system can be described by an effective non-Hermitian Hamiltonian ($\hbar = 1$):

$$H_{\text{eff}} = J(|0\rangle\langle 1| + |1\rangle\langle 0|) - 2i\gamma|1\rangle\langle 1|, \tag{1}$$

where J is the coupling rate and γ is the dissipation rate. It can be mapped to the non-Hermitian $\mathcal{PT}$-symmetric Hamiltonian in equation (1) by adding an identity matrix $H_{PT} = H_{\text{eff}} + i\gamma \boldsymbol{I}$. H_{PT} describes a balanced gain and loss two-level system. To calibrate this $\mathcal{PT}$-symmetric system, we measured the eigenvalue spectrum, quantum fisher information, and phase diagram of the non-unitary dynamics, which are included in appendix B.

2.2. QSL on the non-Hermitian Bloch sphere

From the geometric point of view, the QSL in a Hermitian system can be obtained using the Fubini-Study metric method, i.e. the geodesic line in the Hilbert space [38, 39]. In order to extend the geometric treatment to a non-Hermitian system, we need to build a variant Bloch sphere. We first write down a general $\mathcal{PT}$-symmetric Hamiltonian with

$$H_{PT} = \begin{pmatrix} i\gamma & Je^{i\phi_J} \\ Je^{-i\phi_J} & -i\gamma \end{pmatrix}, \tag{2}$$

where ϕ_J is the phase of the driving field. A linear operator $\mathcal{C}$, which commutes with both the Hamiltonian H and the operator $\mathcal{PT}$, and $\mathcal{C}^2 = 1$, can be defined. Then, a new form of inner product $\langle a|b\rangle^{\mathcal{CPT}} = (\mathcal{CPT}a)\cdot b$ can be constructed, where the complex conjugate is replaced by the $\mathcal{CPT}$-conjugate [40–42]. For a certain $|\psi\rangle$, the value of the new inner product can be written as $\langle\psi|\psi\rangle^{\mathcal{CPT}} = \langle\psi|\mathcal{P}^T\mathcal{C}^T|\psi\rangle$.

Using the $\mathcal{CPT}$ conjugate, the eigenstates $|\varepsilon_{\pm}\rangle$ of H_{PT} in equation (2) become a set of complete orthogonal basis. We are then motivated to use this basis to construct the new Bloch sphere, which depends on the operator $\mathcal{C}$ with

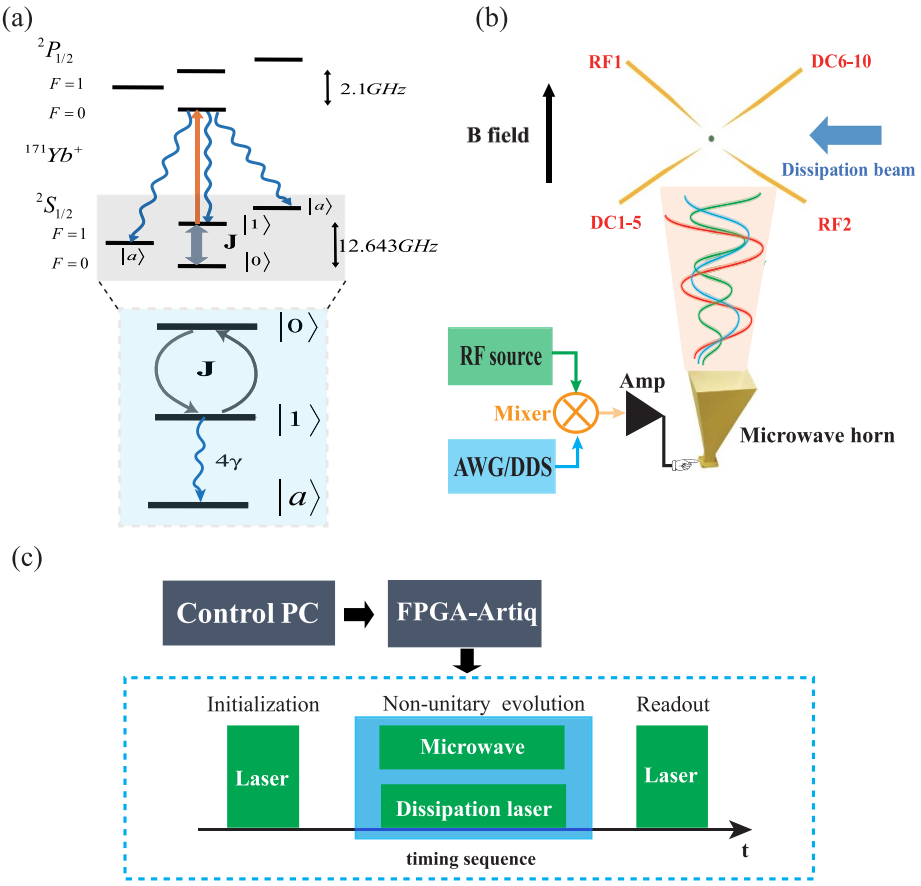

Figure 1. The experimental system of a passive non-Hermitian $\mathcal{PT}$-symmetric Hamiltonian. (a) The related energy levels of a $^{171}Yb^+$ ion . The involved five levels, $|F=0,m_F=0\rangle$ and $|F=1,m_F=0,\pm1\rangle$ in the electronic ground state $^2S_{1/2}$ and $|F=0,m_F=0\rangle$ in the electronic excited state $^2P_{1/2}$, can be simplified to a three-level non-Hermitian system with $|0\rangle=|^2S_{1/2},F=0,m_F=0\rangle$, $|1\rangle=|^2S_{1/2},F=1,m_F=0\rangle$ and $|a\rangle=|^2S_{1/2},F=1,m_F=\pm1\rangle$, where the population on $|1\rangle$ dissipates to $|a\rangle$ with a rate of 4γ. (b) The schematic diagram of the experimental setup. The magnetic (B) field, the dissipation beam and the microwave (MW) are illustrated. (c) The timing sequences in the experiment.

$$\mathcal{C}=\frac{1}{\sqrt{1-\left(\frac{\gamma}{J}\right)^2}}\begin{pmatrix} ie^{-i\phi_J}\frac{\gamma}{J} & 1 \\ 1 & -ie^{i\phi_J}\frac{\gamma}{J}\end{pmatrix}. \tag{3}$$

For $\phi_J=0$, this definition of $\mathcal{C}$ is reduced to the formula suggested in [41].

Based on equation (3), we establish a mapping between a Hermitian Bloch sphere and a $\mathcal{PT}$-symmetric non-Hermitian Bloch sphere, which can be described as $f:|\psi\rangle\rightarrow|\psi\rangle^{\mathcal{CPT}}$. The state $|\psi\rangle=\cos\frac{\theta}{2}|0\rangle+e^{i\phi}\sin\frac{\theta}{2}|1\rangle$ is well described in a normal Hermitian Bloch sphere with the orthogonal basis $|0\rangle$ and $|1\rangle$. In $\mathcal{CPT}$-conjugate Hilbert space, using $|\varepsilon_+\rangle$ and $|\varepsilon_-\rangle$ as the basis, $|\psi\rangle^{\mathcal{CPT}}$ can be written as

$$|\psi\rangle^{\mathcal{CPT}}=R\cos\frac{\Theta}{2}|\varepsilon_+\rangle+R\sin\frac{\Theta}{2}e^{i\Phi}|\varepsilon_-\rangle, \tag{4}$$

where R, Θ and Φ are functions of θ, ϕ and ϕ_J : $R=R(\theta,\phi,\phi_J),\Theta=\Theta(\theta,\phi,\phi_J),\Phi=\Phi(\theta,\phi,\phi_J)$. More details can be found in appendix C.

By fixing the value of R to $\sqrt{\langle1|1\rangle^{\mathcal{CPT}}}$, a $\mathcal{PT}$-symmetric non-Hermitian Bloch sphere can be constructed, where $|1\rangle^{\mathcal{CPT}}$ evolves under unitary evolution. We note that the $\mathcal{PT}$-symmetric non-Hermitian Bloch sphere can be regarded as the generalized Hermitian Bloch sphere under the distorted effect due to the dissipation. This is illustrated in figure 2(a), when $\gamma=0$, the Hamiltonian in equation (2) becomes Hermitian, and the non-Hermitian Bloch sphere turns into a Hermitian Bloch sphere. It is noted that a special case of the non-Hermitian Bloch sphere with $\phi_J=0$ has been constructed in [17].

As γ gradually increases, due to the effect of C operator, the non-Hermitian Bloch sphere gets more and more distorted. With the distortion, the geodesic 'distance' between $|0\rangle$ and $|1\rangle$ becomes shorter and shorter with increasing γ/J, as shown in figures 2(b)–(d). As γ/J approaches the unity, i.e. the exceptional point, the 'distance' become infinitesimally small.

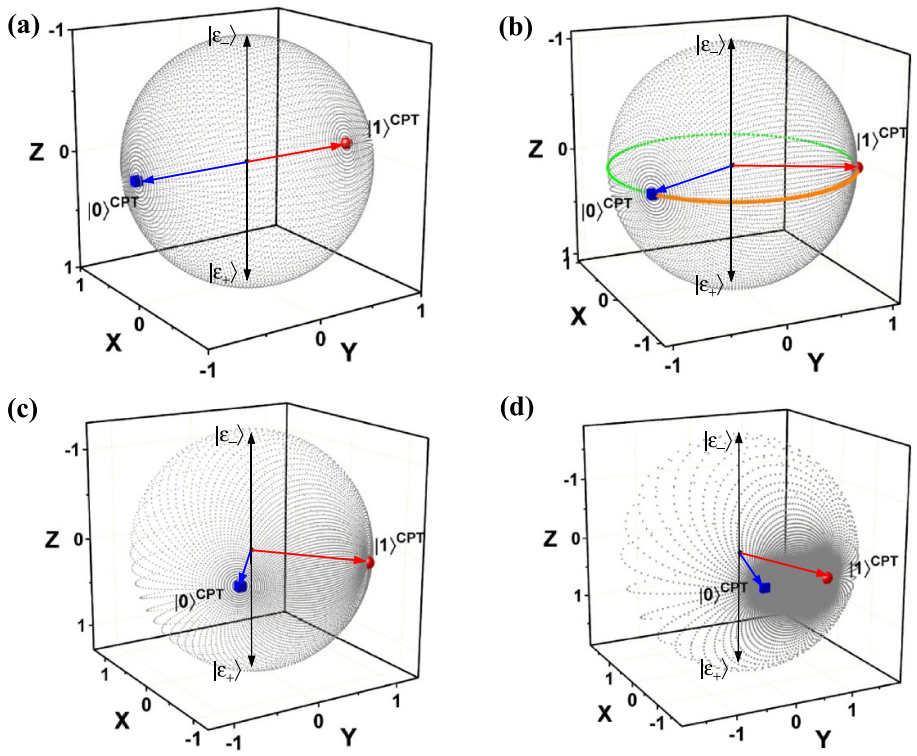

Figure 2. The non-Hermitian $\mathcal{PT}$ symmetry Bloch sphere mapped from the Hermitian Bloch sphere. The red sphere (blue cube) represents $|1\rangle^{\mathcal{CPT}}(|0\rangle^{\mathcal{CPT}})$ mapped from state $|1\rangle(|0\rangle)$ described in the Hermitian case. We scan θ from 0 to $\pi/2$ and ϕ from 0 to 2π, taking 10 100 points on average in the Hermitian Bloch sphere. The values of γ are (a) 0, (b) 0.48J, (c) 0.80J and (d) 0.96J, respectively. The orange and green curves in (b) represent the trajectories of the evolution from $|1\rangle$ to $|0\rangle$ and from $|0\rangle$ to $|1\rangle$, respectively.

The distorted sphere also shows chiral dependence of the evolution time on the path. The evolution makes a longer trip along the geodesic line on the opposite direction as illustrated in figure 2(b). From the geometrical point of view, the whole period for a round trip from state $|1\rangle$ to $|0\rangle$, and back to $|1\rangle$, should not be smaller than two fold of the Margolus–Levitin bound in the Hermitian case [43]. This dissipation induced distortion of the Bloch sphere is in analogy to the distortion of space-time by the gravitation field in Einstein's general theory of relativity, which is dubbed as the *wormholelike effect* in [28].

The QSL of a non-Hermitian system had been investigated by various methods, but still remains an open question [20, 25, 26, 44]. Here, we give the ML- and MT-type QSL using two different methods for the $\mathcal{PT}$-symmetric Hamiltonian of equation (2). For the ML bound, [26] provides $\tau_{\rm ML} \geqslant \frac{\hbar}{2E_\tau}\sin^2[\mathcal{L}(|\psi_0\rangle, |\psi_\tau\rangle)]$ using the Bures metric for a closed system, where $E_\tau = \frac{1}{\tau}\int_0^\tau \langle H_t\rangle \, {\rm d}t$ is the time-averaged energy and $\mathcal{L}(|\psi_0\rangle, |\psi_\tau\rangle) = \arccos|\langle\psi_0|\psi_\tau\rangle|$ defines the geodesic length between the initial state $|\psi_0\rangle$ and the final state $|\psi_\tau\rangle$ of the quantum system. These formula can be applied to the $\mathcal{PT}$-symmetric Hamiltonian using the $\mathcal{CPT}$ symmetry framework [45]. Following the $\mathcal{CPT}$ symmetry defined above, if the system evolves from the state $|1\rangle$ to the final state $|\psi_\tau\rangle = (\cos(\theta_\tau/2), \sin(\theta_\tau/2)) = |0\rangle$, we have

$$\tau_{ML} = \frac{(\pi - 2\arcsin(\gamma/J))\hbar}{2J\sqrt{1-(\gamma/J)^2}}, \tag{5}$$

with detailed derivation in appendix F. For the MT bound, [25] provides the bound of $\tau_{\rm MT} \geqslant \frac{2\sqrt{2}\theta^2 Tr(\rho_0{}^2)}{\pi\sqrt{Tr[(\mathcal{L}_s^\dagger\rho)^2]}}$, which is based on relative purity metric. $\mathcal{L}_s$ is the time-dependent super operator with $\mathcal{L}_s\rho = \frac{{\rm d}\rho}{{\rm d}t}$, and ρ_0 is the initial state. For the system evolving from the state $|1\rangle$ to the final state $|0\rangle$, $\theta = \pi/2$ giving

$$\tau_{MT} = \frac{\pi\hbar}{2\sqrt{J^2+2\gamma^2}} \tag{6}$$

also with the derivation in appendix F.

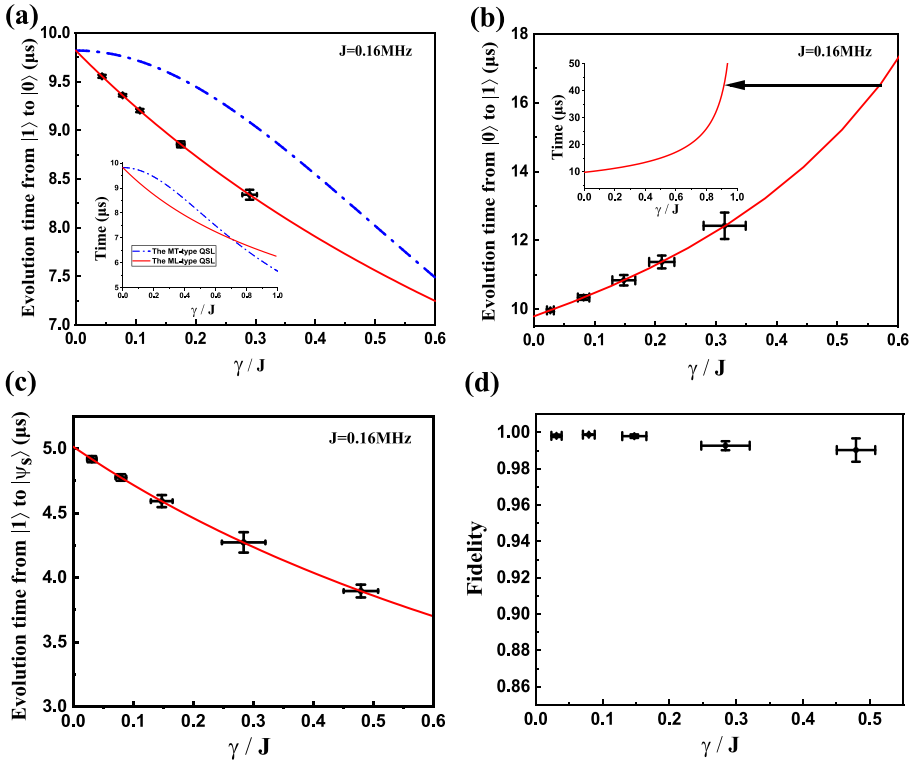

Figure 3. The non-Herimitian state transfer of a trapped-ion qubit. The dependence of the evolution time from (a) $|1\rangle$ to $|0\rangle$, (b) $|0\rangle$ to $|1\rangle$, and (c)$|1\rangle$ to $|\psi_s\rangle$ on the γ/J. The coupling strength $J \approx 0.16$ MHz in (a)–(c). The black circles and the error bars are obtained from the experiment data. The red line in (a), (c) and (b) correspond to the theoretical estimation from equations (5) and (8), respectively. The dashed blue line in (a) correspond to the theoretical estimation from equation (6), which is not a tight bound for our case. The inset pictures in (a) and (b) show the theoretical evolution time for the extended range of $\gamma/J \in [0, 1]$. (d) The fidelities of the final states obtained from quantum state tomography for five different γ/J in (c).

2.3. Experimental demonstration of QSL in the $\mathcal{PT}$ system

In a trapped-ion qubit, the coupling rate J and the dissipation rate γ can be adjusted by tuning the intensity of the microwave and the dissipation beam, respectively. Initially, the system is prepared in the $|1\rangle$. After a certain time τ of the non-unitary evolution, the population in $|1\rangle$ becomes

$$\rho_{11}(\tau) = \mathrm{e}^{-2\gamma\tau}\left[\cos(\chi\tau) - \frac{\gamma\sin(\chi\tau)}{\chi}\right]^2, \tag{7}$$

where $\chi = \sqrt{J^2 - \gamma^2}$. The equation (7) can be obtained from the effective Hamiltonian of equation (1), where $\rho_{11}(\tau) = |\langle 1|\exp(-iH_{\mathrm{eff}}\tau)|1\rangle|^2$. In appendix D, a detailed derivation of equation (7) is also given by the Lindblad master equation. The coupling rate J can be determined from the measurement of Rabi oscillation. For a fixed J, the dissipation rate γ can be obtained by fitting the population curve according to equation (7).

We measure τ_{ML} under the different dissipation intensities γ/J and find excellent agreement with the theoretical predictions, as shown in figure 3(a). When $\gamma/J = 0$, the Hamiltonian reduces to Hermitian, and $\tau_{\mathrm{ML}} = \tau_{\mathrm{MT}} = \pi\hbar/2J$, corresponding to the Rabi flipping time with a unitary evolution. As the dissipation strength is increased ($0 < \gamma < J$), the evolution time becomes smaller and smaller.

As shown in figure 3(a), the experimental data agree well with the ML bound τ_{ML} (the red solid line). It is noted that the MT bound τ_{MT} (the blue dash line) is higher than the ML bound τ_{ML} in the regime of $\gamma/J < 0.7$, indicating the MT bound of equation (6) based on the relative purity metric is not a tight bound for our system. For the larger dissipation $\gamma/J > 0.7$ (the inset of figure 3(a)), τ_{MT} provides a tighter bound, but experimental data of the flipping time is lacking due to the degraded signal-to-noise ratio (SNR) resulted from the large dissipation. For the experimentally accessible region, because $\tau_{\mathrm{exp}} = \tau_{\mathrm{ML}}$, then the ML-type QSL is successfully reached by our experiments.

We investigate the chiral dependence of the flipping time τ_f', where the system evolves along the opposite direction from $|0\rangle$ to $|1\rangle$. Its flipping time follows

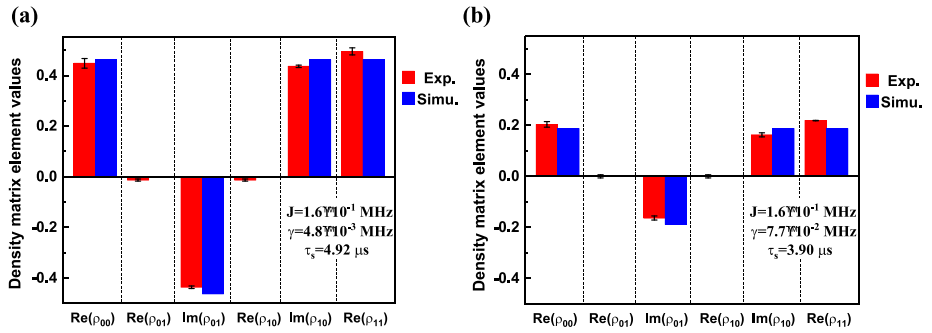

Figure 4. The non-Hermitian quantum state tomography. The comparison between experimentally and numerically reconstructed density matrix for (a) $\gamma/J = 0.03$, $\tau_s = 4.92\,\mu s$ and (b) $\gamma/J = 0.48$, $\tau_s = 3.90\,\mu s$, which correspond to the first and fifth point in figure 3(c). Each density matrix is averaged five times, and in each time every element of the density matrix consists of ten measurements. The red bars are the experimental results, and the blue bars are the simulation results.

$$\tau_f' = \frac{\pi + 2\arcsin\left(\frac{\gamma}{J}\right)}{2J\sqrt{1-\left(\frac{\gamma}{J}\right)^2}}, \tag{8}$$

which gets longer with larger γ/J, as shown in figure 3(b).

We also perform the qubit rotation from the initial state $|1\rangle$ to the normalized superposition state $|\psi_s\rangle = \frac{1}{\sqrt{2}}(|1\rangle - i|0\rangle)$. By measuring the time-dependent population in $|1\rangle$ and fitting it according to equation (7), the evolution time τ_s is acquired, as shown in figure 3(c). The speedup effect is also observed. The flipping time τ_s becomes smaller and smaller as γ increases.

In order to quantify the coherence of the non-unitary evolution, we have measured the fidelity of the non-Hermitian state transfer for each operation. This is done by preparing the qubit to $|\psi_{\rm exp}\rangle$, where τ_s is precisely set for the applied duration of dissipated laser and microwave. The theoretical $|\psi_{\rm th}\rangle$ is solved from $|\psi_{\rm th}\rangle = e^{-iH_{\rm eff}\tau_s/\hbar}|1\rangle$. Its corresponding density matrix $\rho_{\rm exp} = |\psi_{\rm exp}\rangle\langle\psi_{\rm exp}|$ is reconstructed and measured with the quantum state tomography, whose details is described in appendix E. Then, the fidelity $F = \frac{|Tr[\bar{\rho}_{\rm th}\bar{\rho}_{\rm exp}]|}{\sqrt{Tr[\bar{\rho}_{\rm th}^2]Tr[\bar{\rho}_{\rm exp}^2]}}$ is obtained [46–48], where $\bar{\rho} = \frac{\rho(t)}{Tr[\rho(t)]}$. In figure 4, the comparison of the density matrix between the theory and the experimental results for $\gamma/J = 0.03$ ($\tau_s = 4.92\,\mu s$) and $\gamma/J = 0.48$ ($\tau_s = 3.90\,\mu s$) are illustrated, respectively. The measurements agree with the theoretical calculations well.

In figure 3(d), the fidelities for small dissipation strength $\gamma/J < 0.2$, are close to the unity. These data indicate that when the dissipation is small, the non-Hermitian approximation remains valid as discussed in appendix D. So the dynamics could reserve excellent quantum coherence under the non-Hermitian Hamiltonian. The non-Hermitian dynamics avoids the decoherence by disregarding the quantum jump terms, which ensures the coherence regardless of the dissipation. But the significant error arises for the larger $\gamma/J > 0.2$, as shown in figures 3(b) and (c). The increase of the error with the dissipation strength is due to the fact that the approximation of non-Hermitian Hamiltonian get worse when the dissipation is large, and we need consider the decoherence induced by the quantum jump term. On the other hand, we use a purely dissipative system to map the balanced gain-loss one, where the population exponentially decays over time, as illustrated in figures B2(b) and (c). The fast reduction in population leads to the decrease in the SNR of the data for the larger dissipation rate. This limitation hinders the high fidelity data when increasing $\gamma/J > 0.5$. The additional technical issues in the experiments include the large fluctuation of the laser beam intensity and the stray magnetic field. These can be addressed by employing feedback control of the laser intensity and the dynamical decoupling sequences [49].

2.4. Speedup with the anti-$\mathcal{PT}$ Hamiltonian

In order to confirm such non-Hermitian induced speedup is also valid for an anti-$\mathcal{PT}$-symmetric Hamiltonian, we measure the state evolution from $|\varphi_1\rangle$ to $|\varphi_2\rangle$ using an anti-$\mathcal{PT}$-symmetric Hamiltonian, as illustrated by the purple geodesic line in figure 5(a). To solve the brachistochrone problem with the anti-$\mathcal{PT}$-symmetric Hamiltonian, we define a new series of the non-Hermitian operators as $A_1 = i\sigma_x'/2$, $A_2 = i\sigma_y'/2$, $A_3 = i\sigma_z'/2$, which satisfy the structure of the Lie algebra $\mathfrak{su}(2) = \langle A_1, A_2, A_3 : [A_1, A_2] = A_3, [A_3, A_1] = A_2, [A_2, A_3] = A_1\rangle$, with

$$\sigma_x' = |\varepsilon_-\rangle\langle\varepsilon_+| + |\varepsilon_+\rangle\langle\varepsilon_-| = \begin{pmatrix} 0 & i \\ -i & 0 \end{pmatrix}, \tag{9}$$

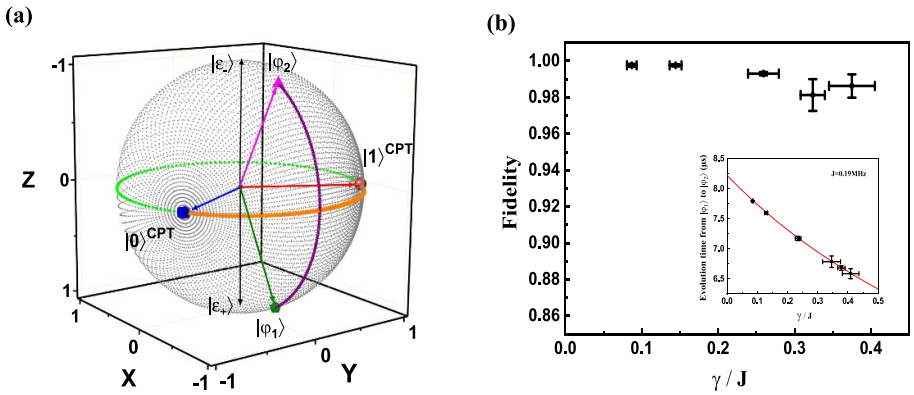

Figure 5. The trajectories on the non-Hermitian Bloch sphere. (a) The green pentagon and magenta triangle represent $|\varphi_1\rangle = \frac{|0\rangle^{CPT}+|1\rangle^{CPT}}{\sqrt{2}}$ and $|\varphi_2\rangle = \frac{|0\rangle^{CPT}-|1\rangle^{CPT}}{\sqrt{2}}$, respectively. The purple trajectory indicates the evolution from $|\varphi_1\rangle$ to $|\varphi_2\rangle$. The simulation parameter $\gamma = 0.09$ MHz, $J = 0.19$ MHz. (b) The fidelities of the state transfer operation along purple trajectory in (a), the experimental data is obtained from quantum state tomography for five different γ/J. Each density matrix is averaged five times, and in each time every element of the density matrix consists of ten measurements. The insert picture in (b) is the flipping time from $|\varphi_1\rangle$ to $|\varphi_2\rangle$ under different γ/J.

$$\sigma_y' = i|\varepsilon_+\rangle\langle\varepsilon_-| - i|\varepsilon_-\rangle\langle\varepsilon_+| = \frac{1}{\sqrt{J^2-\gamma^2}}\begin{pmatrix} J & -i\gamma \\ -i\gamma & -J \end{pmatrix}, \tag{10}$$

$$\sigma_z' = |\varepsilon_+\rangle\langle\varepsilon_+| - |\varepsilon_-\rangle\langle\varepsilon_-| = \frac{1}{\sqrt{J^2-\gamma^2}}\begin{pmatrix} i\gamma & J \\ J & -i\gamma \end{pmatrix}, \tag{11}$$

where σ_z' is a $\mathcal{PT}$-symmetric operator, and σ_y' is an anti-$\mathcal{PT}$-symmetric operator. The rotation operator $U' = \exp(-i\boldsymbol{n}\cdot\boldsymbol{\sigma'}/2)$ is defined on the non-Hermitian Bloch sphere, where $\boldsymbol{\sigma'} = (\sigma_x', \sigma_y', \sigma_z')$. Note that the unitary of the rotation is still guaranteed by the $\mathcal{CPT}$ conjugate defined with the anti-$\mathcal{PT}$-symmetric Hamiltonian.

The anti-$\mathcal{PT}$-symmetric Hamiltonian is constructed experimentally by adding extra microwave pulses using the method shown in our previous work [33]. We measure the transition from $|\varphi_1\rangle = \frac{|0\rangle^{CPT}+|1\rangle^{CPT}}{\sqrt{2}}$ to $|\varphi_2\rangle = \frac{|0\rangle^{CPT}-|1\rangle^{CPT}}{\sqrt{2}}$. It can be viewed as a rotation around the Y axis on the non-Hermitian Bloch sphere, as shown in figure 5(a), which is symmetric to the orange geodesic line. The fidelity maintains a high value when γ/J is less than 0.3 shown in figure 5(b).

3. Conclusions

We have experimentally realized a faster-than-Hermitian state transfer using a trapped-ion qubit with $\mathcal{PT}$-symmetric and anti-$\mathcal{PT}$-symmetric Hamiltonians. The evolution time gets shorter with the increasing dissipation strength, which approaches the QSL of the ML bound associated with the non-Hermitian Hamiltonian. This QSL can be well explained with non-Hermitian Bloch sphere using the Bures angle metric. Meanwhile, the fidelity of the quantum state evolution remains above 98% when the dissipation strength is relatively small.

The presented QSL offers a novel perspective for achieving optimal quantum control [45, 50]. We have constructed the $\mathcal{CPT}$-symmetric Bloch sphere, giving a geometric interpretation for the QSL in the non-Hermitian quantum systems. Enabled by the rotation operators in the Lie group, the optimal state preparation and evolution in the presence of the dissipation can be designed. The shortest trajectory along the geodesic line, i.e. the QSL can always be achieved, by choosing an appropriate set of operators satisfying the structure of the Lie algebra. Many potential applications can be envisioned, e.g. the extension of the single-qubit non-Hermitian Bloch sphere to N-qubit case [51], which could facilitate a better understanding of N-qubit gate operation in open quantum systems.

Furthermore, the QSL under non-Hermitian conditions provides a potential solution for seeking novel precision measurement approaches. There exists the intrinsic relation between the QSL with the quantum Fisher information and the quantum Cramér-Rao bound [25, 52], so the precision of measurement is

directly related to the speed of dynamics. Approaching the QSL could enhance the precision of quantum measurement in a non-Hermitian system.

In the end, the exploration of the QSL could help to resolve many intriguing questions in open systems [53], such as whether the speedup of state transfer could also enhance the rate of generating entanglement, whether the energy cost of the state transfer is minimized by reaching the QSL, etc.

Data availability statement

All data that support the findings of this study are included within the article (and any supplementary files).

Acknowledgments

This work is supported by the Key-Area Research and Development Program of Guangdong Province under Grant No. 2019B030330001, the National Natural Science Foundation of China under Grant Nos. 11974434 and 12074439, Natural Science Foundation of Guangdong Province under Grant 2020A1515011159, Science and Technology Program of Guangzhou, China 202102080380, the Shenzhen Science and Technology Program under Grant Nos.2021Szvup172, JCYJ20220818102003006, and Guangdong Science and Technology Project under Grant No. 20220505020011. Le Luo acknowledges the support from Guangdong Province Youth Talent Program under Grant No. 2017GC010656.

Appendix A. Experimental setup for non-Hermitian trapped-ion qubits

A single $^{171}Yb^{+}$ ion is confined and laser cooled in a linear Paul trap consisting of four gold-plated ceramic blade electrodes. The schematics of the blade trap are shown in figure 1(b). The radio frequency (RF) signal and direct current (DC) voltages are applied to two RF electrodes (RF1 and RF2) and two DC electrodes, respectively. Each DC electrode is divided into five segments so that there are more degrees of freedom to manipulate the ion. We define the trap axis as **x** axis, other two axes perpendicular to the trap axis as **y** and **z** axis. The trap has an axial trap frequency of $\nu_x = 2\pi \times 0.744$ MHz and two radial trap frequency of $(\nu_y, \nu_z) = (2\pi \times 1.382\,\text{MHz}, 2\pi \times 1.655\,\text{MHz})$. In the system, a pair of Helmholtz coils create a magnetic field around 6 Gauss along vertical **z** axis, which not only shifts the degeneracy of the three magnetic levels, but also prevents the ion from getting pumped into a coherent dark state. The microwave signal for driving the qubit rotation consists of a 12.611 580 GHz signal from standard RF source (Rohde and Schwarz, SMA 100B) and a 31.25 MHz signal from an arbitrary waveform generator (AWG, Spectrum Instrumentation). The relative phase of the microwave is precisely controlled by the input functions and parameters on the AWG. A 1 GHz signal from standard RF source is used as the AWG reference.

For the timing control, the switching of the cooling laser, pumping laser, dissipation beam, and detection beam are all controlled by switching the acoustic-optic modulators (AOM, Brimose TEM-200-50-369) with RF switches (Mini-Circuits, ZASWA-2-50DR+), to which TTL (Transistor–Transistor Logic) signals are fed from ARTIQ (Advanced Real-Time Infrastructure for Quantum physics) device (M-Labs, Sinara Kasli). The synchronization of the microwave and the dissipation beam is precisely controlled. The intensity of the dissipation beam can be tuned by adjusting the RF power applied on the AOM.

Appendix B. The properties of $\mathcal{PT}$-symmetric Hamiltonian

We investigate the $\mathcal{PT}$ symmetry breaking transition. In figures B1(a) and (b), the evolution of the eigenvalues in a passive $\mathcal{PT}$ system is shown with γ for a constant J. At $\gamma = 0$, the system is a Hermitian system and has two real eigenvalues. As it increases from 0 to J, the imaginary part of the eigenvalue $\text{Im}[\lambda]$ appears and decreases linearly with $-i\gamma$ from 0, while two real parts $\text{Re}[\lambda]$ follow the upper and lower halves of the circle $\sqrt{J^2-\gamma^2}$ and gradually converge. At $\gamma = J$, $\text{Re}[\lambda] = 0$ and $\text{Im}[\lambda] = -\gamma$, this is so-called the exceptional point (EP). When it further increases, the real part stays 0, whereas the imaginary part separates into two modes, one is slow decay mode (upper branch) and follows the hyperbolic line according to $-\gamma + \sqrt{\gamma^2 - J^2}$, while the other is fast decay mode (lower branch) and follows the hyperbolic line according to $-\gamma - \sqrt{\gamma^2 - J^2}$. The region of $0 \leqslant \gamma < J$ is defined as $\mathcal{PT}$-symmetric phase, whereas the region of $\gamma > J$ is defined as $\mathcal{PT}$-broken phase. The overlap between two eigenstates $|\alpha\rangle$ and $|\beta\rangle$ in both $\mathcal{PT}$-symmetric and $\mathcal{PT}$-broken region, which satisfies $|\langle\alpha|\beta\rangle| = \min(\gamma/J, J/\gamma)$, is shown in figure B1(c). Near the EP point, the two eigenstates of Hamiltonian coalesce into one.

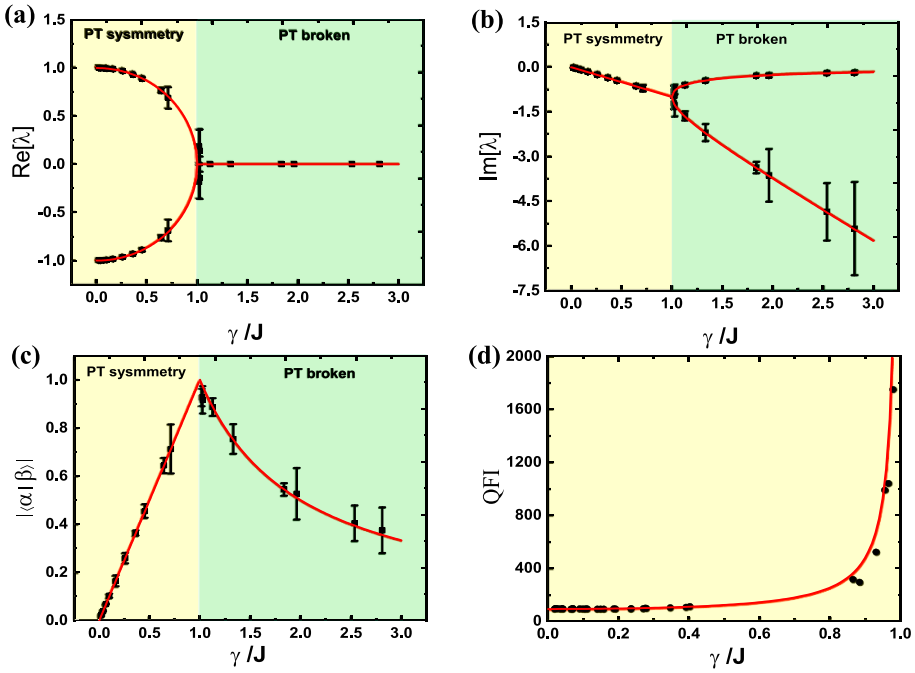

Figure B1. The real part (a) and the imaginary part (b) of the eigenvalues. In both (a) and (b), the rectangles represent the experimental data, while the red line represents the theoretical solution. In (b), the imaginary part in the $\mathcal{PT}$-symmetric phase is negative and decreases with $-i\gamma$ due to a passive $\mathcal{PT}$-symmetric system. It separates into a slow (upper branch) and a fast(lower branch) decay mode in the $\mathcal{PT}$-broken phase. (c) The overlap between the two eigenstates $|\alpha\rangle$ and $|\beta\rangle$ in both $\mathcal{PT}$-symmetric and $\mathcal{PT}$-broken phases, satisfying $|\langle\alpha|\beta\rangle| = \min(\gamma/J, J/\gamma)$ (red line). (d) The theoretical quantum Fisher information (QFI) of damping rate $F = \frac{2}{J^2-\gamma^2}$ (red line) for $J > \gamma$, compared with the experimental measurement (black circles).

In addition, the eigenstates of the non-Hermitian Hamiltonian H_{eff} can be used for measuring γ. The explicit formula of the quantum Fisher information (QFI) for the two-dimensional density matrices is written as [54]:

$$\mathcal{F}_\gamma = \mathrm{Tr}\left(\partial_\gamma \rho\right)^2 + \mathrm{Tr}\left(\rho \partial_\gamma \rho\right)^2 / \det \rho. \tag{B.1}$$

It can be used to obtain the QFI of damping rate $F = \frac{2}{J^2-\gamma^2}$ for $J > \gamma$, as is shown in figure B1(d). As γ approaches J, the magnitude of QFI goes to infinity. We show here the location of the EP can be precisely determined by utilizing this feature of QFI. One can also employ this feature to obtain a very good precision of damping rate γ [55] by tuning the coupling strength J to EP. It is worth to notice, the enhanced sensitivity near the EP bears similarities to weak value amplification [56, 57].

Then, we directly measure the density matrix elements of $\rho_{00}(t)$ by performing non-Hermitian evolution, thus obtaining the population in $|0\rangle$ state. Color maps of the population on $|0\rangle$ versus t for various dissipation strengths γ are shown in figure B2(a). The evolution dynamics of the population is further studied by comparing it in $\mathcal{PT}$-symmetric phase (figure B2(b)) with the one in $\mathcal{PT}$-broken phase (figure B2(c)). In figure B2(b), red squares, blue circles, green diamonds and yellow hexagons correspond to $\gamma/J = 0.04$, 0.07, 0.16 and 0.26, respectively. When γ increases with respect to J, the population shows a damping oscillation with the damping proportional to the strength of the γ. In figure B2(c), red squares, blue circles, green diamonds and yellow hexagons correspond to $\gamma/J = 1.06$, 1.16, 1.87 and 2.40, respectively. In $\mathcal{PT}$-broken phase, the population decays in a single exponential form and it decays slower with larger γ/J. It is also evident, the dynamical behavior changes from damping oscillations to exponential decay with increasing γ, when the system transits from $\mathcal{PT}$-symmetric phase to $\mathcal{PT}$-broken phase.

Since the passive $\mathcal{PT}$-symmetric system and the $\mathcal{PT}$-symmetric system with balanced gain and loss share the same topological features, they have one-to-one correspondence according to equation (2) of the main text. Thus, the investigations of the former system offer the ability to explore the dynamics of the latter system [58]. Consequently, the dynamical process such as the evolution of the population in the dissipative $\mathcal{PT}$-symmetric system can be accurately mapped to a balanced gain and loss $\mathcal{PT}$-symmetric system through the relation $\rho^{\mathcal{PT}}(t) = e^{2\gamma t}\rho(t)$. The mapped population dynamics in the balanced gain and loss $\mathcal{PT}$-symmetric system are shown in figures B2(d) and (e). In figure B2(c), the evolution of population in $|0\rangle$ state with time for $\gamma/J = 0.1$ in dissipative $\mathcal{PT}$-symmetric phase is mapped to a $\mathcal{PT}$-symmetric system with balanced gain and loss. Similarly, in figure B2(d), the evolution of population in $|0\rangle$ state with time for

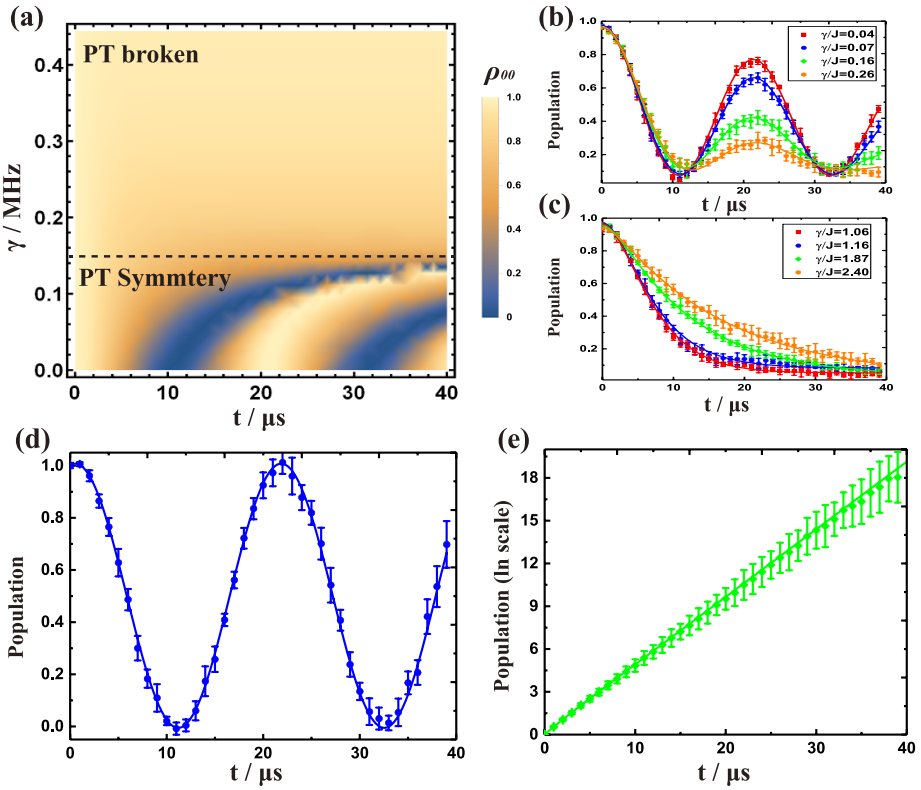

Figure B2. (a) Color maps of the population on $|0\rangle$ versus t for various dissipation strengths γ. In our system, the coupling between $|0\rangle$ and $|1\rangle$ is kept at $J = 0.148$ MHz. The evolution of the population in $|0\rangle$ with time for different γ/J in both dissipative $\mathcal{PT}$-symmetric phase (b) and $\mathcal{PT}$-broken phase (c), illustrating the evolution dynamics between $|0\rangle$ and $|1\rangle$. In (b), red squares, blue circles, green diamonds and yellow hexagons correspond to $\gamma/J = 0.04$, 0.07, 0.16 and 0.26, respectively. In (c), red squares, blue circles, green diamonds and yellow hexagons correspond to $\gamma/J = 1.06$, 1.16, 1.87 and 2.40, respectively. (d) The evolution of the population in $|0\rangle$ with time for $\gamma/J = 0.07$ in dissipative $\mathcal{PT}$-symmetric phase is mapped to $\mathcal{PT}$-symmetric system with balanced gain and loss, since both of the systems share the same topological features. (e) The evolution of $|0\rangle$ state with time for $\gamma/J = 1.87$ in passive $\mathcal{PT}$-broken phase is mapped to $\mathcal{PT}$-symmetric system with balanced gain and loss.

$\gamma/J = 1.87$ in dissipative $\mathcal{PT}$-broken phase is mapped. It can be clearly seen, the population dynamics in $|0\rangle$ for $\gamma/J = 0.07$ retains a Rabi-oscillation-like profile after mapping. However, the population dynamics in $|0\rangle$ for $\gamma/J = 1.87$ displays an exponential increase with time.

Appendix C. The mapping of $\mathcal{PT}$-symmetric non-Hermitian Bloch sphere

For a $\mathcal{PT}$-symmetric Hamiltonian which has specific phase ϕ_J in the off-diagonal terms (equation (2)). By defining $\alpha \equiv \arcsin\frac{\gamma}{J}$, the eigenstates of equation (2) become:

$$|\varepsilon_+\rangle = \sqrt{\frac{J}{\Delta E}}\begin{pmatrix} e^{i\phi_J}e^{i\alpha/2} \\ e^{-i\alpha/2}\end{pmatrix}, \quad |\varepsilon_-\rangle = \sqrt{\frac{J}{\Delta E}}\begin{pmatrix} ie^{i\phi_J}e^{-i\alpha/2} \\ -ie^{i\alpha/2}\end{pmatrix} \tag{C.1}$$

where $\Delta E \equiv 2\sqrt{J^2-\gamma^2}$ is defined as the difference between two eigenvalues. State $|\psi\rangle = \cos\frac{\theta}{2}|0\rangle + e^{i\phi}\sin\frac{\theta}{2}|1\rangle$ can be represented with the basis of $|\varepsilon_+\rangle$ and $|\varepsilon_-\rangle$:

$$|\psi\rangle = m_1\left(\theta,\phi,\frac{\gamma}{J},\phi_J\right)|\varepsilon_+\rangle + m_2\left(\theta,\phi,\frac{\gamma}{J},\phi_J\right)|\varepsilon_-\rangle \tag{C.2}$$

where m_1 and m_2 are complex numbers

$$\begin{aligned} m_1\left(\theta,\phi,\frac{\gamma}{J},\phi_J\right) &= \sqrt{\frac{J}{\Delta E}}\left[e^{-\frac{i\alpha}{2}}e^{i\phi}\sin(\theta/2) + e^{\frac{i\alpha}{2}}e^{-i\phi_J}\cos(\theta/2)\right], \\ m_2\left(\theta,\phi,\frac{\gamma}{J},\phi_J\right) &= \sqrt{\frac{J}{\Delta E}}\left[ie^{\frac{i\alpha}{2}}e^{i\phi}\sin(\theta/2) - ie^{-\frac{i\alpha}{2}}e^{-i\phi_J}\cos(\theta/2)\right]. \end{aligned} \tag{C.3}$$

Thus, the state can be rewritten as:

$$|\psi\rangle = r_1e^{i\Phi_1}|\varepsilon_+\rangle + r_2e^{i\Phi_2}|\varepsilon_-\rangle \tag{C.4}$$

where

$$r_1 = \sqrt{\frac{1+\sin(\theta)\cos(\alpha-\phi-\phi_J)}{2\cos(\alpha)}},$$
$$r_2 = \sqrt{\frac{1-\sin(\theta)\cos(\alpha+\phi+\phi_J)}{2\cos(\alpha)}}. \tag{C.5}$$

As $|\psi\rangle$ in equation (C.4) is a four parameters vector, by extracting a common phase, $|\psi\rangle$ turns into:

$$|\psi\rangle^{\mathcal{CPT}} = R\cos\frac{\Theta}{2}|\varepsilon_+\rangle + R\sin\frac{\Theta}{2}e^{i\Phi}|\varepsilon_-\rangle \tag{C.6}$$

where $R \equiv \sqrt{{r_1}^2+{r_2}^2}$, $\Phi \equiv \Phi_2 - \Phi_1$ and $\Theta \equiv 2\arcsin(\sqrt{\frac{1-\sin(\theta)\cos(\alpha+\phi+\phi_J)}{2+2\sin(\alpha)\sin(\theta)\sin(\phi+\phi_J)}})$. This helps us deriving the distribution of the state represented by Bloch sphere in $\mathcal{CPT}$-conjugate inner product space. Moreover, the evolution operator $U_{H_{\mathcal{PT}}} = e^{-iH_{\mathcal{PT}}t/\hbar}$ become unitary by setting $R = \sqrt{\langle\psi_0|\psi_0\rangle^{\mathcal{CPT}}}$, where $|\psi_0\rangle$ is the initial state. In the main context, $R = \sqrt{\langle 1|1\rangle^{\mathcal{CPT}}}$ because the system is initialized to $|1\rangle$. Consequently, a non-Hermitian Bloch sphere have been constructed.

Appendix D. Lindblad evolution of the five-level system

In the physical process described in the paper, the population of a qubit with $|0\rangle = |F=0, m_F=0\rangle$ and $|1\rangle = |F=1, m_F=0\rangle$ dissipates via a pumping laser to state $|4\rangle = |F=0, m_F=0\rangle$ in ${}^2P_{1/2}$, which then decays rapidly to the state $|1\rangle$ and $|a\rangle = |2,3\rangle = |F=1, m_F=\pm1\rangle$ in ${}^2S_{1/2}$ with the decay rate $\gamma_0 = \gamma_1+\gamma_2+\gamma_3$ ($\gamma_1 \approx \gamma_2 \approx \gamma_3 = 2\pi\times 19.6$ MHz). Such an evolution of the qubit can be obtained by numerically solving the master equation of the involved five energy levels: ($\hbar = 1$):

$$\frac{\mathrm{d}\rho}{\mathrm{d}t} = -i[H_C,\rho] + \sum_{k=0,1}\left(L_k\rho {L_k}^\dagger - \frac{1}{2}\{{L_k}^\dagger L_k,\rho\}\right), \tag{D.1}$$

where $\rho(t)$is a 5×5 density matrix, $\frac{d\rho}{dt}$ is the time derivative, $H_C = J_m|0\rangle\langle 1| + J_l|1\rangle\langle 4| + h.c$ represents the sum of the microwave coupling between $|0\rangle$ and $|1\rangle$ and the laser coupling between $|1\rangle$ and $|4\rangle$ in the rotating frame. L_k is the Lindblad dissipation operator with $L_1 = \sqrt{\gamma_1}|1\rangle\langle 4|$, $L_2 = \sqrt{\gamma_2}|2\rangle\langle 4|$ and $L_3 = \sqrt{\gamma_3}|3\rangle\langle 4|$. The dagger represents the Hermitian conjugate.

Because the microwave drive and the dissipation laser beam only act on the qubit, the dynamics of $|a\rangle$ is decoupled from qubit states, therefore we focus on the qubit subspace of the whole system, where the qubit retains its coherence and its dynamics is governed by an effective $\mathcal{PT}$-symmetric Hamiltonian H_{eff} in an approximated three-level system model as illustrated in figure 1(a) of the main text. The condition of the approximation is that the coupling strength between state $|1\rangle$ and $|4\rangle$ is much smaller than the linewidth of the level $|4\rangle$. The comparison of the evolution of the entire five-level master equation and the evolution of the effective $\mathcal{PT}$-symmetric Hamiltonian is shown in the figure D1. The qubit evolution in this approximated three-level system can be described by the following Lindblad master equation ($\hbar = 1$):

$$\frac{\mathrm{d}\rho}{\mathrm{d}t} = -i[H_{C1},\rho] + \left(L_1\rho {L_1}^\dagger - \frac{1}{2}\{{L_1}^\dagger L_1,\rho\}\right), \tag{D.2}$$

where $\rho(t)$ is a 3×3 density matrix, $H_{C1} = J(|1\rangle\langle 0| + |0\rangle\langle 1|)$ is a coupling Hamiltonian. $L_1 = \sqrt{4\gamma}|a\rangle\langle 1|$ is the dissipation operator which accounts for the population probability decay from level $|1\rangle$ to $|a\rangle$, where 4γ is the effective dissipation rate from $|1\rangle$ to $|a\rangle$ with $\gamma = J_l^2(\gamma_0-\gamma_1)/\gamma_0^2$. By omitting the quantum jump term in equation (D.2), the qubit dynamics is given by the following equations:

$$\frac{d\rho}{dt} = \begin{pmatrix} iJ(\rho_{01}(t)-\rho_{10}(t)) & i(J\rho_{00}(t)+2i\gamma\rho_{01}(t)-J\rho_{11}(t)) \\ -2\gamma\rho_{10}(t)-iJ(\rho_{00}(t)-\rho_{11}(t)) & -iJ(\rho_{01}(t)-\rho_{10}(t))-4\gamma\rho_{11}(t) \end{pmatrix}. \tag{D.3}$$

When the system was initialized in the $|1\rangle$ state, the population in each qubit state can be obtained by solving equation (D.3). In addition, when we regroup equation (D.2), we can get the below expression:

$$\frac{\mathrm{d}\rho}{\mathrm{d}t} = -i\left[\left(H_{C1} - \frac{i}{2}{L_1}^\dagger L_1\right)\rho - \rho\left(H_{C1} + \frac{i}{2}{L_1}^\dagger L_1\right)\right] + L_1\rho {L_1}^\dagger \tag{D.4}$$

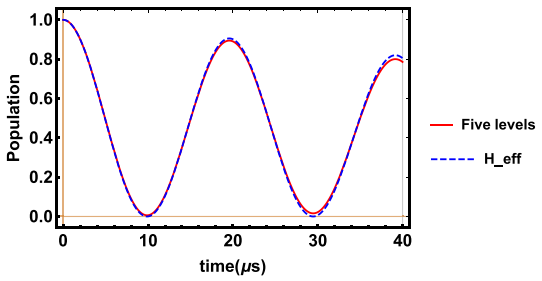

Figure D1. The comparison of the evolution of the master equation of the entire 5-level and the evolution of the effective Hamiltonian. The red solid curve and the blue dashed curve represent the numerical solution of the five-level master equation and the solution of the effective two-level Hamiltonian, respectively. The simulation parameters are $J_m = 2\pi \times 26$ KHz, $J_l = 2\pi \times 189$ KHz, $\gamma = 2\pi \times 0.4$ KHz.

When we also discard the quantum jump term $L_1 \rho {L_1}^\dagger$, we can get the effective non-Hermitian Hamiltonian $H_{\text{eff}} = H_{C1} - \frac{i}{2}{L_1}^\dagger L_1$. This is the equation (1) in main text. Likewise, the population in state $|0\rangle$ and $|1\rangle$ can be obtained from the effective Hamiltonian H_{eff}, where

$$\begin{aligned}\rho_{00}(\tau) &= |\langle 0|\exp(-iH_{\text{eff}}\tau)|1\rangle|^2 = \frac{e^{-2\gamma t}J^2\sin(\chi t)^2}{\chi^2} \\ \rho_{11}(\tau) &= |\langle 1|\exp(-iH_{\text{eff}}\tau)|1\rangle|^2 = e^{-2\gamma t}\left[\cos(\chi t) - \frac{\gamma\sin(\chi t)}{\chi}\right]^2,\end{aligned} \tag{D.5}$$

where $\chi = \sqrt{J^2 - \gamma^2}$. Experimentally, the population on state $|0\rangle$ ($|1\rangle$) was fit to the exponentially decaying sine function in equation (D.5) to determine the decay rate and the Rabi oscillation frequency.

Appendix E. Non-Hermitian quantum state tomography

The 2×2 density matrix $\hat{\rho}$ can always be represented by:

$$\hat{\rho} = \frac{1}{2}\sum_{i=0}^{3} S_i \hat{\sigma}_i \tag{E.1}$$

where the $\hat{\sigma}_i$ matrices are $\hat{\sigma}_0 = \begin{pmatrix}1 & 0\\ 0 & 1\end{pmatrix}$, $\hat{\sigma}_1 = \begin{pmatrix}0 & 1\\ 1 & 0\end{pmatrix}$, $\hat{\sigma}_2 = \begin{pmatrix}0 & -i\\ i & 0\end{pmatrix}$, $\hat{\sigma}_3 = \begin{pmatrix}1 & 0\\ 0 & -1\end{pmatrix}$, and the S_i values are given by $S_i = Tr\{\hat{\sigma}_i\hat{\rho}\}$. Physically, each of these parameters directly corresponds to the outcome of a specific pair of projective measurements:

$$\begin{aligned} S_0 &= P_{|0\rangle} + P_{|1\rangle} \\ S_1 &= P_{\frac{1}{\sqrt{2}}(|0\rangle+|1\rangle)} - P_{\frac{1}{\sqrt{2}}(|0\rangle-|1\rangle)} \\ S_2 &= P_{\frac{1}{\sqrt{2}}(|0\rangle+i|1\rangle)} - P_{\frac{1}{\sqrt{2}}(|0\rangle-i|1\rangle)} \\ S_3 &= P_{|0\rangle} - P_{|1\rangle} \end{aligned} \tag{E.2}$$

where $P_{|\psi\rangle}$ is the probability to measure the state $|\psi\rangle$. We need to measure the population of these six basis vectors in the experiment because the sum of $P_{|0\rangle}$ and $P_{|1\rangle}$ is not the unity under non-Hermitian evolution. The experimental procedures to obtain the density matrix are listed below.

(1) For measuring the population of $P_{|0\rangle}$, we first prepare the system in the initial state $|1\rangle$. After time t of non-unitary evolution, we detect the state $|0\rangle$. (2) For measuring the population of $P_{|1\rangle}$, we first prepare the system in the initial state $|1\rangle$. After time t of non-unitary evolution, we add an appropriate π flip to exchange the population of the state $|0\rangle$ and $|1\rangle$ of the hyperfine manifold. Finally, we detect the total population of state $|1\rangle$ and $|a\rangle$, and the initial population of state $|1\rangle$ can be inferred from the unity population of all states. (3) For measuring the population of $P_{\frac{1}{\sqrt{2}}(|0\rangle+i|1\rangle)}$, we first prepare the system in the initial state $|1\rangle$. After time t of non-unitary evolution, we add an appropriate $\pi/2$ flip. Finally, we detect the state $|0\rangle$ to get $P_{\frac{1}{\sqrt{2}}(|0\rangle+i|1\rangle)}$. (4) For measuring the population of $P_{\frac{1}{\sqrt{2}}(|0\rangle-i|1\rangle)}$, we first prepare the system in the initial state $|1\rangle$. After time t of non-unitary evolution, we add an appropriate $\pi/2$ flip. Finally, we detect the state $|0\rangle$ to get $P_{\frac{1}{\sqrt{2}}(|0\rangle-i|1\rangle)}$. (5) For measuring the population of $P_{\frac{1}{\sqrt{2}}(|0\rangle-|1\rangle)}$, we first prepare the system in the initial state $|1\rangle$. After time t of non-unitary evolution, we add an appropriate $\pi/2$ flip. Finally, we detect the state $|0\rangle$ to get $P_{\frac{1}{\sqrt{2}}(|0\rangle-|1\rangle)}$.

(6) For measuring the population of $P_{\frac{1}{\sqrt{2}}(|0\rangle+|1\rangle)}$, we first prepare the system in the initial state $|1\rangle$. After time t of non-unitary evolution, we add an appropriate $\pi/2$ flip. Finally, we detect the state$|0\rangle$ to get $P_{\frac{1}{\sqrt{2}}(|0\rangle+|1\rangle)}$.

Appendix F. The derivation of both ML and MT-type QSL

The ML bound based on the method using Bures metric. For a driven closed system, the ML bound is written as $\tau_{\mathrm{ML}} \geqslant \frac{\hbar}{2E_\tau}\sin^2[\mathcal{L}(\rho_0,\rho_\tau)]$ [26], where $E_\tau = \frac{1}{\tau}\int_0^\tau \langle H_t\rangle \,\mathrm{d}t$ is the time-averaged energy , and $\mathcal{L}(\rho_0,\rho_\tau) = \arccos\sqrt{\langle\psi_0|\rho_\tau|\psi_0\rangle}$ $(\mathcal{L}(|\psi_0\rangle,|\psi_\tau\rangle) = \arccos|\langle\psi_0|\psi_\tau\rangle|)$ defining the geodesic length between the initial state and the final state of the quantum system. Considering the state evolution represented by the time-dependent θ_t, the average energy E_τ can be rewritten as $E_\tau = \frac{1}{\theta_\tau-\theta_0}\int_0^{\theta_\tau-\theta_0}\langle H_{\theta_t}\rangle \,\mathrm{d}\theta_t$, where

$$\langle H_{\theta_t}\rangle = \left(|Tr\{H\rho_t\rho_0\}| + |Tr\{\rho_t H\rho_0\}|\right)/2 \tag{F.1}$$

$$H = \begin{pmatrix} 0 & E_+ \\ E_+ & 0 \end{pmatrix}. \tag{F.2}$$

In our system, given the initial state $|\psi_0\rangle(\theta_0,\phi_0)$ and the final state $|\psi_\tau\rangle(\theta_\tau,\phi_\tau)$, $|\phi_\tau-\phi_0| = 0$ if we define appropriate coordinate and $|\langle\psi_0|\psi_\tau\rangle| = \cos(\frac{|\theta_\tau-\theta_0|}{2})$. In this work, we start from the state $|1\rangle$ to the final state $|\psi_\tau\rangle(\cos(\theta_\tau/2),\sin(\theta_\tau/2))$. The time-averaged energy $E_\tau = \frac{1}{\theta_\tau-\theta_0}\int_0^{\theta_\tau-\theta_0} E_+\cos(\theta_t/2)\sin(\theta_t/2)\mathrm{d}\theta_t$, where $E_+ = \sqrt{J^2-\gamma^2}$ is the energy gap. Considering boundary condition that $E_0 = 0$, we can get the ML bound under driven dynamics $\tau_{\mathrm{ML}} = \frac{\hbar(\theta_\tau-\theta_0)}{2E_+}$. In the Hilbert space of non-Hermitian dynamics, the ML-type QSL from $|1\rangle$ to $|0\rangle$ can be expressed as

$$\tau_{\mathrm{ML}} = \frac{(\pi - 2\arcsin(\gamma/J))\hbar}{2J\sqrt{1-(\gamma/J)^2}}, \tag{F.3}$$

where $\theta_\tau-\theta_0$ equals $\pi - 2\arcsin(\gamma/J)$, which describes the angle between $|1\rangle$ and $|0\rangle$ in non-Hermitian Hilbert space. Noting that this angle is smaller than π as the two states lose orthogonality, as shown in figure 2 of the main text. It is also noted that, according to [45], for this specific $\mathcal{PT}$-symmetric Hamiltonian, the Bures angle method will make the MT type bound coincident with the ML bound.

The evolution time by solving quantum brachistochrone problem . The evolution operator of effective $\mathcal{PT}$-symmetric non-Hermitian Hamiltonian can be written as

$$U = e^{-iH_{\mathrm{eff}}t} = \begin{pmatrix} e^{-t\gamma}\left(\cos[t\chi] + \frac{\gamma\sin[t\chi]}{\chi}\right) & -\frac{ie^{-t\gamma}J\sin[t\chi]}{\chi} \\ -\frac{ie^{-t\gamma}J\sin[t\chi]}{\chi} & e^{-t\gamma}\left(\cos[t\chi] - \frac{\gamma\sin[t\chi]}{\chi}\right) \end{pmatrix}, \tag{F.4}$$

where $\chi = \sqrt{J^2-\gamma^2}$.

To solve this problem, one can choose the basis so that the initial and final states are given by: $|\psi_i\rangle = \begin{pmatrix} 0 \\ 1 \end{pmatrix}$, $|\psi_f\rangle = \begin{pmatrix} a \\ b \end{pmatrix}$. Here, the system is initialized in the $|1\rangle$ state. The relation $|\psi_f\rangle = e^{-iH_{\mathrm{eff}}t}|\psi_i\rangle$ $(\hbar = 1)$ takes the form

$$\begin{pmatrix} a \\ b \end{pmatrix} = \frac{\mathrm{e}^{-t\gamma}}{\cos\left[\arcsin\left[\frac{\gamma}{J}\right]\right]}\begin{pmatrix} -i\sin\left[t\sqrt{J^2-\gamma^2}\right] \\ \left(\cos\left[t\sqrt{J^2-\gamma^2}+\arcsin\left[\frac{\gamma}{J}\right]\right]\right) \end{pmatrix}. \tag{F.5}$$

If $b = 0$, the evolution time from $|1\rangle$ to $|0\rangle$ can be deduced

$$t = \frac{\pi - 2\arcsin\left[\frac{\gamma}{J}\right]}{2J\sqrt{1-\left(\frac{\gamma}{J}\right)^2}} \tag{F.6}$$

which is exactly the same as τ_{ML}.

The MT bound based on the method of relative purity metric. The relative purity [25] between the initial state ρ_0 and the final state ρ_t is defined as $f(t) = \mathrm{Tr}(\rho_0\rho_t)/\mathrm{Tr}(\rho_0^2)$. The maximum instantaneous evolution rate of the system satisfies

$$\nu_{QSL} = |\mathrm{d}f(t)/\mathrm{d}t| \leqslant \frac{\sqrt{Tr\left[\left(\mathcal{L}_s^\dagger\rho_0\right)^2\right]}}{Tr[\rho_0^2]}, \tag{F.7}$$

where $\mathcal{L}_s$ is the time-dependent super operator. Let $f(t)=\cos\theta(\theta\in[0,\pi/2])$ and consider $f(t)\leqslant\int_0^t\nu_{\rm QSL}{\rm d}t'$, then we can obtain $\tau_{\rm MT}\geqslant\frac{4\theta^2{\rm Tr}(\rho_0{}^2)}{\pi^2\sqrt{{\rm Tr}[(\mathcal{L}_s^\dagger\rho)^2]}}$.

When the initial and final states are orthogonal pure states, the expression $\tau_{\rm MT}$ is given by $\tau_{\rm MT}=\frac{\hbar}{\sqrt{2}\Delta E}$ $(\theta=\pi/2)$. However, we can find that this expression must multiply by a factor $\pi/\sqrt{2}$ to return to the closed system MT type boundary $\tau_{MT}=\frac{\pi\hbar}{2\Delta E}$. Similarly, in open systems under non-Hermitian Hamiltonian

$$H_{eff}=\begin{pmatrix}i\gamma & J\\ J & i\gamma\end{pmatrix}=\begin{pmatrix}0 & J\\ J & 0\end{pmatrix}-i\begin{pmatrix}\gamma & 0\\ 0 & \gamma\end{pmatrix}=H-i\Gamma, \tag{F.8}$$

where H and Γ are both Hermitian operators, so that $\mathcal{L}_s\rho=-i[H,\rho]/\hbar-\{\Gamma,\rho\}/\hbar$. Finally, the MT bound can be obtained by multiply a factor $\pi/\sqrt{2}$ to the Mandelstam–Tamm relation

$$\begin{aligned}\tau_{\rm MT}&\geqslant\frac{\pi}{\sqrt{2}}\frac{4\theta^2Tr\left(\rho_0^2\right)}{\pi^2\sqrt{Tr\left[\left(\mathcal{L}_s^\dagger\rho\right)^2\right]}}\\&=\frac{4\theta^2Tr\left(\rho_0^2\right)\hbar}{\pi\sqrt{2Tr\left(-[H,\rho]^2-\{\Gamma,\rho\}^2-2i[H,\Gamma]\rho^2\right)}}\\&=\frac{4\theta^2\hbar}{2\pi\sqrt{\Delta H^2+(\langle\Gamma^2\rangle+\langle\Gamma\rangle^2)-i\langle[H,\Gamma]\rangle}}\\&=\frac{\pi\hbar}{2\sqrt{J^2+2\gamma^2}},\end{aligned} \tag{F.9}$$

where $\theta=\pi/2$. This is then used as a MT type QSL for open quantum systems and compared with our experimental data.

ORCID iD

Le Luo https://orcid.org/0000-0002-8375-6326

References

[1] Lloyd S 2000 *Nature* **406** 1047–54
[2] Campaioli F, Yu C-S, Pollock F A and Modi K 2022 *New J. Phys.* **24** 065001
[3] Aifer M and Deffner S 2022 *New J. Phys.* **24** 055002
[4] Yung M-H 2006 *Phys. Rev.* A **74** 030303
[5] Giovannetti V, Lloyd S and Maccone L 2011 *Nat. Photon.* **5** 222–9
[6] Chin A W, Huelga S F and Plenio M B 2012 *Phys. Rev. Lett.* **109** 233601
[7] Deffner S and Lutz E 2010 *Phys. Rev. Lett.* **105** 170402
[8] Campbell C, Li J, Busch T and Fogarty T 2022 *New J. Phys.* **24** 095001
[9] Takahashi K 2022 *New J. Phys.* **24** 065004
[10] Mandelstam L and Tamm I 1991 The uncertainty relation between energy and time in non-relativistic quantum mechanics *Selected Papers* (Springer) pp 115–23
[11] Pfeifer P 1993 *Phys. Rev. Lett.* **70** 3365
[12] Ness G, Lam M R, Alt W, Meschede D, Sagi Y and Alberti A 2021 *Sci. Adv.* **7** eabj9119
[13] Hörnedal N, Allan D and Sönnerborn O 2022 *New J. Phys.* **24** 055004
[14] Margolus N and Levitin L B 1998 *Physica* D **120** 188–95
[15] Levitin L B and Toffoli T 2009 *Phys. Rev. Lett.* **103** 160502
[16] Mostafazadeh A 2007 *Phys. Rev. Lett.* **99** 130502
[17] Günther U and Samsonov B F 2008 *Phys. Rev.* A **78** 042115
[18] Günther U and Samsonov B F 2008 *Phys. Rev. Lett.* **101** 230404
[19] Assis P E and Fring A 2008 *J. Phys. A: Math. Theor.* **41** 244002
[20] Taddei M M, Escher B M, Davidovich L and de Matos Filho R L 2013 *Phys. Rev. Lett.* **110** 050402
[21] Marvian I and Lidar D A 2015 *Phys. Rev. Lett.* **115** 210402
[22] Funo K, Shiraishi N and Saito K 2019 *New J. Phys.* **21** 013006
[23] Lan K, Xie S and Cai X 2022 *New J. Phys.* **24** 055003
[24] Mohan B, Das S and Pati A K 2022 *New J. Phys.* **24** 065003
[25] del Campo A, Egusquiza I L, Plenio M B and Huelga S F 2013 *Phys. Rev. Lett.* **110** 050403
[26] Deffner S and Lutz E 2013 *Phys. Rev. Lett.* **111** 010402
[27] Nakajima S and Utsumi Y 2022 *New J. Phys.* **24** 095004
[28] Bender C M, Brody D C, Jones H F and Meister B K 2007 *Phys. Rev. Lett.* **98** 040403
[29] Brody D C and Longstaff B 2019 *Phys. Rev. Res.* **1** 033127
[30] Wang W-C *et al* 2021 *Phys. Rev.* A **103** L020201

[31] Ding L, Shi K, Zhang Q, Shen D, Zhang X and Zhang W 2021 *Phys. Rev. Lett.* **126** 083604
[32] Ding L, Shi K, Wang Y, Zhang Q, Zhu C, Zhang L, Yi J, Zhang S, Zhang X and Zhang W 2022 *Phys. Rev.* A **105** L010204
[33] Bian J, Lu P, Liu T, Wu H, Rao X, Wang K, Lao Q, Liu Y, Zhu F and Luo L 2023 *Fundam. Res.* **3** 904–8
[34] Cimmarusti A, Yan Z, Patterson B, Corcos L, Orozco L and Deffner S 2015 *Phys. Rev. Lett.* **114** 233602
[35] Zheng C, Hao L and Long G L 2013 *Phil. Trans. R. Soc.* A **371** 20120053
[36] Campbell W, Mizrahi J, Quraishi Q, Senko C, Hayes D, Hucul D, Matsukevich D, Maunz P and Monroe C 2010 *Phys. Rev. Lett.* **105** 090502
[37] Guo W-X, Wu Y-K, Huang Y-Y, Feng L, Huang C-X, Yang H-X, Ma J-Y, Yao L, Zhou Z-C and Duan L-M 2022 *Phys. Rev.* A **106** 022608
[38] Anandan J and Aharonov Y 1990 *Phys. Rev. Lett.* **65** 1697
[39] Brody D C 2003 *J. Phys. A: Math. Gen.* **36** 5587
[40] Bender C M, Brody D C and Jones H F 2002 *Phys. Rev. Lett.* **89** 270401
[41] Bender C M 2005 *Contemp. Phys.* **46** 277–92
[42] Bender C M, Brody D C and Jones H F 2004 *Phys. Rev. Lett.* **93** 251601
[43] Giri P R 2008 *Int. J. Theor. Phys.* **47** 2095–100
[44] Cai X and Zheng Y *et al* 2017 *Phys. Rev.* A **95** 052104
[45] Deffner S and Campbell S 2017 *J. Phys. A: Math. Theor.* **50** 453001
[46] Wang X, Yu C-S and Yi X 2008 *Phys. Lett.* A **373** 58–60
[47] Wen J, Qin G, Zheng C, Wei S, Kong X, Xin T and Long G 2020 *npj Quantum Inf.* **6** 1–7
[48] Suter D and Álvarez G A 2016 *Rev. Mod. Phys.* **88** 041001
[49] Bian J, Wang K, Lu P, Rao X, Wu H, Lao Q, Liu T, Liu Y, Zhu F and Luo L 2022 *Phys. Rev.* A **106** 012416
[50] Hegerfeldt G C 2013 *Phys. Rev. Lett.* **111** 260501
[51] Mäkelä H and Messina A 2010 *Phys. Scr.* **2010** 014054
[52] Maleki Y, Ahansaz B and Maleki A 2023 *Sci. Rep.* **13** 12031
[53] Verstraete F, Wolf M M and Ignacio Cirac J 2009 *Nat. Phys.* **5** 633–6
[54] Zhong W, Sun Z, Ma J, Wang X and Nori F 2013 *Phys. Rev.* A **87** 022337
[55] Xie D and Xu C 2019 *Quantum Inf. Process.* **18** 86
[56] Jordan A N, Martínez-Rincón J and Howell J C 2014 *Phys. Rev.* X **4** 011031
[57] Naghiloo M, Abbasi M, Joglekar Y N and Murch K 2019 *Nat. Phys.* **15** 1232–6
[58] Li J, Harter A K, Liu J, de Melo L, Joglekar Y N and Luo L 2019 *Nat. Commun.* **10** 855